

1 **Laboratory data linking the reconfiguration of and drag on individual plants**  
2 **to the velocity structure and wave dissipation over a meadow of salt marshes**  
3 **under waves with and without current**

4 Xiaoxia Zhang<sup>1\*</sup>, Heidi Nepf<sup>2</sup>

5 <sup>1</sup>Water Science and Environmental Engineering Research Center, College of Chemical and  
6 Environmental Engineering, Shenzhen University, Shenzhen, 518060, China

7 <sup>2</sup>Department of Civil and Environmental Engineering, Massachusetts Institute of Technology,  
8 Cambridge, Massachusetts, 02139, USA

9 Correspondence: Xiaoxia Zhang ([xiaoxiazhang@szu.edu.cn](mailto:xiaoxiazhang@szu.edu.cn))

10 **Abstract**

11 Salt marshes provide valuable ecosystem services, which are influenced by their interaction with  
12 current and waves. On the one hand, current and waves exert hydrodynamic force on salt marsh plants,  
13 which shapes the distribution of species within the marsh. On the other hand, the resistance produced by  
14 the plants can shape the flow structure, turbulence intensity, and the wave dissipation over the canopy.  
15 Because marsh plants are flexible structures, their reconfiguration modifies the drag felt by the plants and  
16 the flow. While several previous studies have considered the flexibility of the stem, few studies have  
17 considered the leaf component, which has been shown to contribute the majority of plant resistance. This  
18 paper reports a unique dataset that includes laboratory measurements of both the force on an individual  
19 plant and the flow structure and wave energy dissipation over a meadow of plants. In the individual plant  
20 experiment, the motion of the plant and plant drag, free surface displacement and velocity profile were  
21 measured. The individual plant experiments considered both a live marsh plant (*Spartina alterniflora*) and  
22 a mimic consisting of ten leaves attached to a central stem. For the meadow experiment, velocity profiles  
23 were measured both upstream and within the meadow, and free surface displacement was measured along  
24 the model marsh plant meadow with high spatial and temporal resolution. These experiments used five  
25 water depths (covering both submerged and emergent conditions), three wave periods (from long wave to  
26 short waves), seven wave heights (from linear to nonlinear waves), six current conditions (including pure  
27 current, pure wave, and combined current and waves). In summary, there are 102 individual plant tests and  
28 58 meadow tests. The drag, free surface displacement, and velocity are reported in SMCW.mat file  
29 including the raw data, the phase averages, and the statistical values. A link to the plant motion videos is  
30 also provided. This dataset provides high quality measurements that can be used to develop and validate  
31 models of plant motion, hydrodynamic drag on individual plants, vegetation-generated turbulence, the  
32 evolution of flow structure through a meadow, and the transformation and dissipation of waves over natural  
33 salt marshes. The dataset is available from figshare with detailed instructions for reuse  
34 (<https://doi.org/10.6084/m9.figshare.24117144>; Zhang and Nepf, 2023a).

35 **Keywords:** salt marsh; flexible plant; drag force; reconfiguration; flow structure; wave dissipation;

## 36 1. Introduction

37 Salt marshes are a common feature of coastal and estuary regions, serving as important  
38 habitats and food sources for intertidal invertebrates and small fish (Boesch and Turner, 1984;  
39 Barbier et al., 2011). These marshes also play a crucial role in carbon sequestration, accumulating  
40 carbon stocks at a rate of  $210 \text{ g/cm}^2/\text{year}$ , the highest among all ecosystems on Earth (Pidgeon,  
41 2009). Additionally, salt marshes provide shoreline protection by dissipating extreme waves  
42 (Zhang et al., 2020; Garzon et al., 2019b) and reducing erosion and enhancing sedimentation  
43 (Schoutens et al., 2019; Elschot et al., 2013; Huai et al., 2021). The health and function of salt  
44 marsh ecosystems depend on the interaction between the marsh and surrounding currents and  
45 waves. Currents and waves exert hydrodynamic forces on marsh plants, influencing the  
46 distribution of species within the marsh (Schoutens et al., 2022, 2020). In addition, because marsh  
47 plants are flexible, they reconfigure under hydrodynamic forces, modifying the forces experienced  
48 by the plants (Zhang and Nepf, 2021b), and the impact of plant resistance on flow structure (Chen  
49 et al., 2013; Lowe et al., 2005; Zeller et al., 2015; Lei and Nepf, 2021), turbulence intensity (Xu  
50 and Nepf, 2020), and wave energy transformation (Hu et al., 2014; van Veelen et al., 2020; Vuik  
51 et al., 2016).

52 Theories that quantify the hydrodynamic force on rigid cylinders and flat plates were  
53 developed in the 1950's (Morison et al., 1950; Keulegan and Carpenter, 1958). However, real  
54 plants are flexible and reconfigure under the influence of currents and waves, reducing the  
55 hydrodynamic forces they experience (Luhar and Nepf, 2011; Gosselin et al., 2010; Mullarney and  
56 Henderson, 2010; Zhu et al., 2020). Models have been developed to predict the forces on flexible  
57 structures by considering the reconfiguration and relative motion between the fluid and the plant  
58 (Luhar and Nepf, 2011; Mullarney and Henderson, 2010; Gosselin et al., 2010; Lei and Nepf,  
59 2019b). Laboratory measurements have shown that real plants with different morphologies  
60 followed different scaling laws (Harder et al., 2004; Schutten and Davy, 2000; Jalonen and Järvelä,  
61 2013; Whittaker et al., 2013; Zhang and Nepf, 2020). Many salt marsh plants consist of multiple  
62 flexible leaves attached to single, less flexible central stem, e.g., *Phragmites australis*, *Scirpus*  
63 *maritimus*, *Spartina alterniflora*, and *Spartina anglica*. For these plants, the rigidity and  
64 geometrical properties as well as the density of the leaves and stem affect the drag and hence the  
65 wave dissipation by the plants (Zhu et al., 2023). Zhang and Nepf (2021b) demonstrated that the  
66 force acting on a full model plant can be estimated by summing the forces on all the leaves and

67 the stem, while applying a sheltering coefficient to account for the plant drag reduction due to the  
68 interaction and sheltering among the leaves and the stem. The sheltering coefficient depends on  
69 the geometrical properties of the plant (mainly the distribution of leaves on the stem) and does not  
70 vary with flow conditions. Based on this, predictive models were proposed to estimate the forces  
71 acting on salt marsh plants with both leaves and stem (Zhang and Nepf, 2021b, 2022). The plant  
72 rigidity, morphology, and spatial distribution vary significantly in the field, which makes the  
73 estimation of plant drag and wave dissipation difficult in practice. Fortunately, average values of  
74 plant properties have been shown to produce reasonable estimation for field measurements of wave  
75 dissipation (Zhang and Nepf, 2021b; Zhang et al., 2022, 2021; Zhu et al., 2023).

76 Within a canopy, the presence of plants can significantly alter the flow structure (Chen et al.,  
77 2013; Lowe et al., 2005; Zeller et al., 2015; Lei and Nepf, 2021) and turbulence intensity (Xu and  
78 Nepf, 2020), and reduce wave energy (Garzon et al., 2019a; Zhang et al., 2020; Maza et al., 2015).  
79 The fully developed flow structure within a canopy has been extensively studied under both current  
80 (Chen et al., 2013; Lei and Nepf, 2021) and wave conditions (Lowe et al., 2005) for both emergent  
81 and submerged canopies. Specifically, the mean flow is determined by the distribution of the plant  
82 frontal area for emergent canopies, and by the canopy drag and the ratio of water depth to plant  
83 height for submerged canopies (Nepf, 2012). The wave orbital velocity experiences less  
84 modification by a canopy due to the greater inertial force under waves compared to current (Lowe  
85 et al., 2005), which allows flow motion to penetrate deeper into the lower canopy region. The  
86 presence of plants affects turbulence intensity directly through form drag and wake generated by  
87 plant elements, and indirectly by adjusting the flow structure to create a greater shear and thus  
88 shear production (Nepf, 2012). The resistance of plants can reduce wave height by 30% to 90%  
89 over the first 30 m of a salt marsh (Ysebaert et al., 2011; Knutson et al., 1982; Zhang et al., 2020;  
90 Garzon et al., 2019a), depending on the plant properties (density, geometry, and mechanical  
91 characteristics) and flow conditions (water depth, wave period, wave amplitude, presence of  
92 current). Recent studies proposed simple predictions for wave decay over salt marshes under pure  
93 waves (Zhang et al., 2021, 2022), which has been extended to combined current and wave  
94 conditions using the in-canopy total velocity (Zhang and Nepf, 2021a). However, a well-validated  
95 theoretical model for the time-varying total velocity is currently lacking for salt marshes under  
96 combined current and waves, which hinders the development of accurate models for canopy  
97 turbulence and wave dissipation.

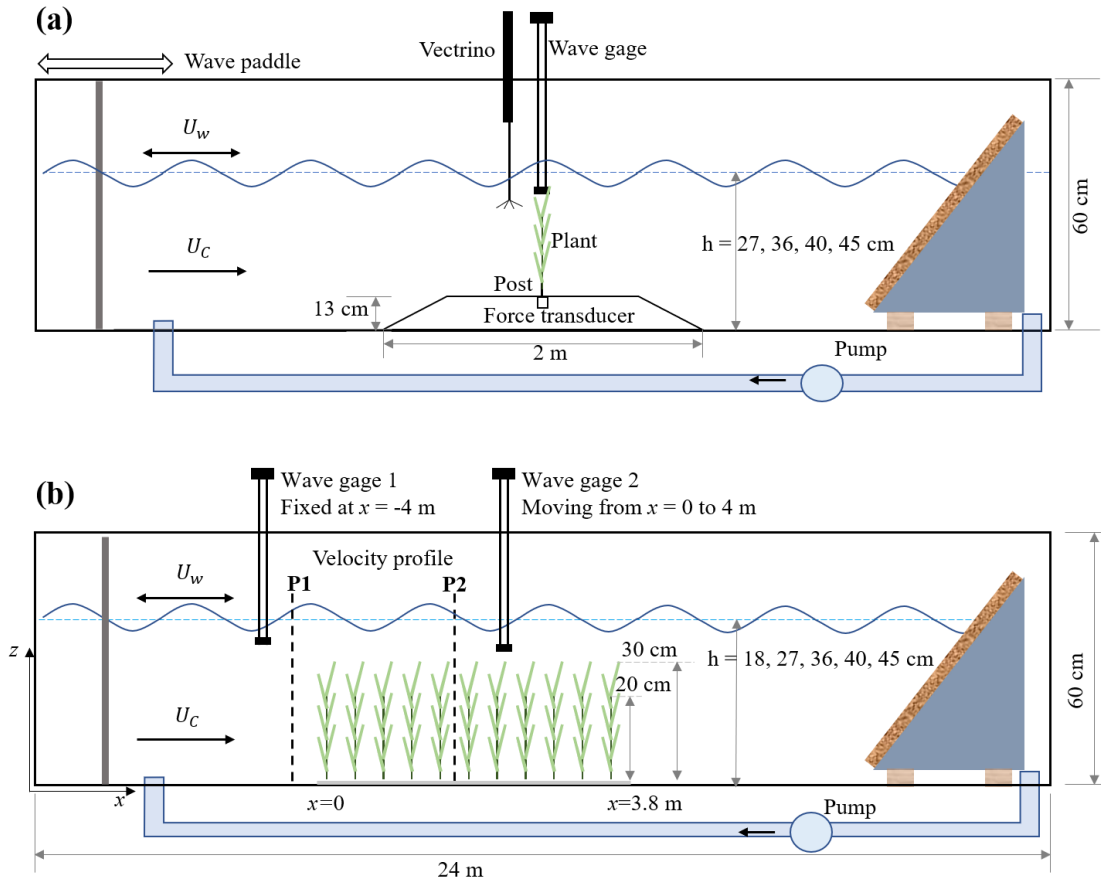
98 This paper presents both force measurements on individual salt marsh plants (Zhang and  
99 Nepf, 2021b, 2022) and measurements of flow structure and wave decay along a meadow of salt  
100 marsh plants (Zhang et al., 2021, 2022; Zhang and Nepf, 2021a). The experiments utilized model  
101 plants that consisted of multiple flexible leaves attached to a central stem, which were designed to  
102 be geometrically and dynamically similar to *Spartina alterniflora*. ~~a common salt marsh~~  
103 ~~species~~The *Spartina spp.* family is distributed widely along the coasts of the Eastern United States,  
104 Europe, South America, and China (see the global distribution in figure 1B in Borges et al., 2021).  
105 The test conditions varied from submerge to emergent, from long to short waves, and from linear  
106 to nonlinear waves with and without following currents. In total, 102 individual plant tests and 58  
107 meadow tests were conducted.

108

## 109 2. Method

110 The experiments were conducted in the Nepf Fluid Mechanics lab at MIT in a 24-m-long, 38-  
111 cm-wide, 60-cm-tall water channel (Fig. 1). The individual plant experiments (denoted by IE, Fig.  
112 1a) provided synchronized measurements of plant drag and free surface displacement, as well as  
113 3-dimensional velocity profiles provided as raw data, phase-averaged data, and statistical data.  
114 Additionally, a link to videos capturing the motion of the plants are provided. The meadow  
115 experiments (denoted by ME, Fig. 1b) provide time-varying measurements of free surface  
116 displacement along the meadow at 10 and 15 cm intervals, as well as velocity profiles upstream of  
117 and within the meadow with 1 to 2 cm vertical resolution. This dataset can facilitate the  
118 development and validation of dynamic marsh plant models, enhance predictions of marsh plant  
119 drag, and deepen our understanding of vegetation-induced turbulence, the evolution of flow  
120 structure within a canopy, and the transformation and dissipation of waves in natural salt marshes.

121 Monochromatic waves were used in all cases, with waves generated with a piston-type  
122 wavemaker. A beach with 1:5 slope and covered with a layer of 10-cm thick coconut fiber was  
123 located at the downstream end of the channel, which limited the wave reflection to  $7\% \pm 3\%$  for  
124 the tested conditions. Following currents (propagating in the same direction as the waves) were  
125 generated by a variable speed pump. Two bricks elevated the beach by 9 cm above the bed to allow  
126 the current to pass.



127

128 **Fig. 1** Schematic of (a) the individual plant experiment (IE) and (b) the meadow experiment (ME),

129 not to scale. The wave paddle and current inlet are at the left, and the wave-absorbing beach at the

130 right. In subplot (a), the model plant was attached to a submersible force sensor housed in a 13-cm

131 high acrylic ramp. A wave gage recorded the free surface displacement at the same longitudinal

132 position as the plant, but 9 cm to the side. A Nortek Vectrino+ measured velocity 10-cm upstream

133 of the plant position, but with the plant removed. In subplot (b), the model meadow was 3.8 m

134 long and located at mid-length along the flume. Two wave gages measured the wave height at a

135 stationary reference position (wave gage 1) and at multiple positions along the meadow (wave

136 gage 2). Velocity in front (P1) and inside the meadow (P2) was measured by Vectrino+.

137

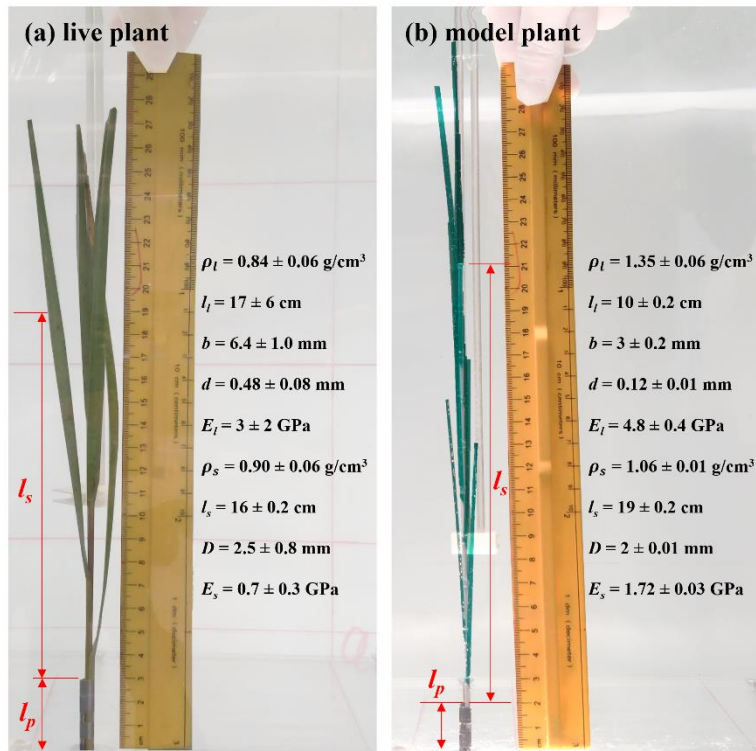
## 138 2.1 Individual plant experiment setup

139 The individual plant experiments (IE) tested a live *Spartina alterniflora*, a single flat plastic

140 leaf, a single cylindrical stem, and a full model marsh plant consisting of 10 leaves attached to a

141 central stem. These tests are labeled as live, leaf, stem, and model, respectively. Fig. 2 shows the

142 live and model plants with the corresponding plant properties (see also Figure 2 and Table 1 in  
 143 Zhang and Nepf, 2021). The live plant consisted of 5 leaves, the dimensions shown in Fig. 2a are  
 144 the mean  $\pm$  SD of these leaves. The plant was attached to a stainless steel post with 2 mm diameter.  
 145 The length of the post above the ramp was  $l_p = 3, 4.5, 2,$  and  $2$  cm for the live, leaf, stem, and  
 146 model plant, respectively. The lower part of the post was attached to a submersible force sensor  
 147 (Futek LSB210 100g), which was mounted beneath an acrylic ramp (1-m top length, 2-m bottom  
 148 length, 13-cm height, and spanning the flume width, see Fig. 1a) to avoid interaction between fluid  
 149 motion and the sensor. IE measured the hydrodynamic force exerted on the plant, the motion of  
 150 the plant, and the associated hydrodynamic conditions (velocity profile and wave height). The  
 151 wave gauge was mounted at the same longitudinal position as the plant, but 9 cm to the lateral side.  
 152 Note that for each plant and each water depth, the zero position of the wave gauge and force sensor  
 153 was determined for still water, i.e., before the wave generator and current pump were turned on.



154  
 155 **Fig. 2** Photos showing (a) the live plant and (b) model plant in the individual plant experiment  
 156 (IE), including a list of plant properties.  $\rho$  is the plant material density, the subscript  $l$  and  $s$  denote  
 157 parameters for the leaves and stem, respectively.  $E$  is the elastic modulus,  $l$  is the element length,  
 158  $b$  and  $d$  are the width and thickness of the leaf.  $D$  is the stem diameter.

159 IE tested 4 water depths  $h = 27, 36, 40,$  and  $45$  cm for the live and full model plant. The leaf  
160 and stem only tests were done under  $h = 45$  cm. Note that the leaf data reported here corresponds  
161 with an initial vertical leaf posture, and the leaf width was oriented perpendicular to the wave  
162 propagation direction (i.e., leaf posture 1 in Figure 4a in Zhang and Nepf, 2021b). Three wave  
163 periods,  $T_w = 2.01, 1.44,$  and  $1.12$  s, and six wave amplitudes were tested. All the tested conditions  
164 are summarized in Table 1, with the case names formed from the type of plant (Live, Leaf, Stem,  
165 Model), the water depth (h27, h36, h40, h45), the wave frequency (f05, f07, and f09), and the wave  
166 height level (W1, W2, W3, W4, W5, W6, W7,  $a_w$  ranging from 0.9 to 4.9 cm). The current  
167 conditions were labeled by pump frequency (10 to 50 Hz), C1, C2, C3, C4, and C5. For example,  
168 Leaf\_h45\_f05\_C1W1 corresponds to the test for an individual model leaf with water depth  $h =$   
169  $45$  cm, and wave period  $T_w = 2.01$  s (wave frequency is 0.5 Hz), current pump frequency set to 10  
170 Hz and the smallest wave height (wave amplitude  $a_w \approx 1$  cm). The tests include the pure wave  
171 experiment reported in Zhang and Nepf (2021) and the combined current and wave experiments  
172 reported in Zhang and Nepf (2022). In addition, there are 23 unreported cases labeled with bold  
173 font case names in Table 1 (6 model plant cases and 17 live plant tests). The new live plant tests  
174 included emergent conditions, which can be used to explore the plant drag dependence on the  
175 degree of submergence. The new model plant cases included a stronger wave condition ( $a_w = 4.7$   
176 cm) and five conditions within the published range of wave height. These new cases expanded the  
177 range of published flow conditions. Across the IE tests, the wave orbital velocity spanned  $U_w = 4$   
178 to  $24$  cm/s, and the channel-average current spanned  $U_c = 3$  to  $18$  cm/s. The current to wave  
179 velocity ratio spanned  $U_c/U_w = 0.16$  to  $4.7$ , covering a range of conditions present in the field  
180 (Garzon et al., 2019b).

181 **Table 1** IE case names with the measured wave amplitudes and the setting current velocity

case names	$a_w \pm 0.1$ cm					$U_c \pm 0.1$ cm/s
<b>Live_h27_f05_W1/W2/W3/W4/W5</b>	1.1	1.8	2.6	1.8	2.3	0
<b>Live_h36_f05_W1/W2/W3/W4/W5/W6/W7</b>	1.0	1.5	2.1	2.9	1.9 2.4 3.0	0
<b>Live_h40_f05_W1/W2/W3/W4/W5</b>	1.0	1.6	2.4	3.2	4.1	0
Live_h45_f05_W1/W2/W3/W4/W5	1.0	1.6	2.0	2.7	3.7	0
Leaf_h45_f05_W1/W2/W3/W4/W5	1.1	1.7	2.4	3.2	4.1	0
Stem_h45_f05_W1/W2/W3/W4/W5	1.0	1.7	2.4	3.3	4.1	0
<b>Model_h27_f05_W1/W2/W3/W4/W5</b>	1.3	2.0	2.7	2.0	2.5	0

Model_h36_f05_W1/W2/W3/W4/ <b>W5/W6/W7</b>	1.0	1.6	2.2	3.1	2.0	2.5	3.1	0
Model_h40_f05_W1/W2/W3/W4/ <b>W5</b>	1.1	1.7	2.4	3.4	4.7			0
Model_h45_f05_W1/W2/W3/W4/W5	0.9	1.5	2.5	3.8	4.2			0
Model_h45_f05_C1W1/W2/W3/W4/W5	1.2	2.0	2.9	4.1	5.2			3.0
Model_h45_f05_C2W1/W2/W3/W4/W5	1.2	2.1	3.0	4.2	5.3			6.8
Model_h45_f05_C3W1/W2/W3/W4/W5	1.2	2.1	3.0	4.1	4.9			10.1
Model_h45_f05_C4W1/W2/W3/W4/W5	1.0	1.7	2.6	3.7	4.8			13.7
Model_h45_f05_C5W1/W2/W3/W4/W5	1.2	2.1	3.0	4.1	5.2			17.6
Model_h45_f07_W1/W2/W3/W4/W5	1.5	2.2	3.1	4.1	6.3			0
Model_h45_f07_C2W1/W2/W3/W4/W5	1.6	2.3	3.2	4.1	6.1			6.8
Model_h45_f07_C4W1/W2/W3/W4/W5	1.1	1.8	2.8	3.7	6.1			13.7
Model_h45_f09_W5	3.0							0
Model_h45_f09_C2W5	2.6							6.8
Model_h45_f09_C4W5	2.2							13.7

182

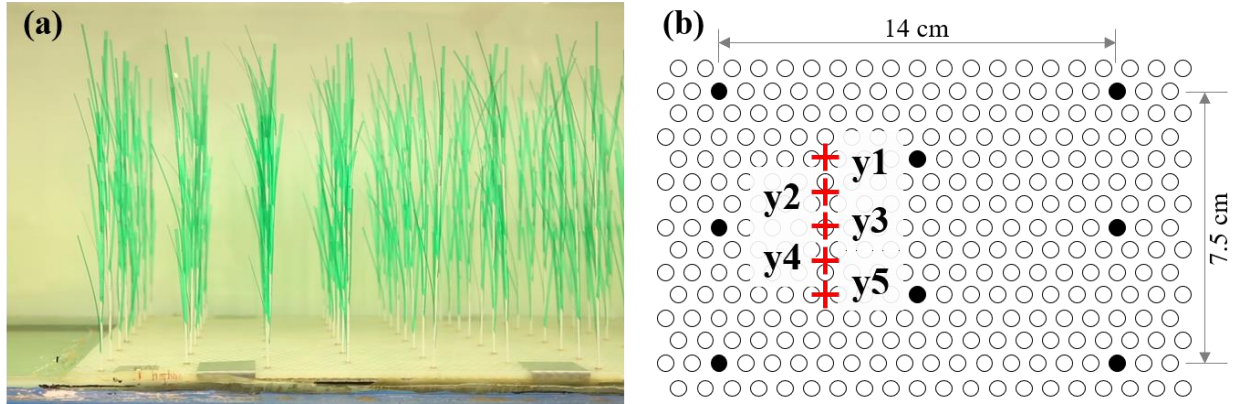
183 The force sensor and wave gauge were controlled by a Labview program which enabled high  
184 quality synchronous measurement. Both the drag force and wave height were measured at a  
185 sampling rate of 2000 Hz and for a duration of 3 minutes. During the force and wave gauge  
186 measurements, a smart cellphone (MIX 2S) camera recorded a 10-second UHD 4k video at 30 fps,  
187 which covered 5 to 10 wave periods, depending on the wave period. The camera was fixed to a  
188 tripod such that the videos for each plant have the same window. The videos for all tests are  
189 available at: <https://doi.org/10.6084/m9.figshare.24117324>. After the force measurements, the  
190 plant and force sensor were removed, and a Nortek Vectrino+ was used to measure the velocity  
191 profile 10 cm upstream of the position where the plant had been to avoid the hole through which  
192 the plant was attached. The vertical resolution of the velocity profile was 1 cm. At each  
193 measurement point, the Vectrino recorded a 3-min record at 200 Hz.

194

## 195 **2.2 Meadow experiment setup**

196 In the meadow experiment (ME), the same model plants used in IE (Fig. 2b) were arranged  
197 in a staggered array with a meadow density of 280 plants/m<sup>2</sup> (Fig. 3). Once inserted, the erect  
198 plants were 30-cm tall. The plants were distributed across the channel width and over a streamwise  
199 distance of 3.8 m.





200  
 201 **Fig. 3** a) Photo of the model plants, b) section of the baseboard with staggered holes (circles) and the plant  
 202 positions within the hole array (filled circles)

203

204 ME tested five water depths,  $h = 18, 27, 36, 40,$  and  $45$  cm, three wave periods,  $T_w = 2, 1.4,$   
 205 and  $1.1$  s, five wave amplitude levels, and three current magnitudes. All the ME cases were  
 206 summarized in Table 2 with the case names ~~were~~ formed based on the flow conditions in the same  
 207 way as IE cases. The flow types include pure current, pure wave, and combined current and wave,  
 208 which were labelled as PC, PW, and CW, respectively. In each case, two wave gages were  
 209 synchronized to measure the free surface displacement at a reference position (wave gauge 1 at  $x = -4$  m)  
 210 and at positions along a transect through the canopy (wave gauge 2). During each  
 211 experimental run (about 90 min), the wave amplitude at wave gauge 1 varied by less than 3%,  
 212 confirming stationary wave conditions. Wave gage 2 collected data between  $x = -4$  to  $4$  m at 10  
 213 and 15 cm intervals. The leading edge of the meadow was located at  $x = 0$ , such that  $x < 0$  was  
 214 over bare bed. At each position, the free surface displacement,  $\eta(t)$ , was recorded at 2000 Hz for  
 215 1 minute. Additional measurements of wave amplitude were made without plants to assess the  
 216 wave decay associated with the channel wall and baseboards alone.

217

218 **Table 2** ME case names with the measured wave amplitudes and the setting current velocity

Flow	case names	aw $\pm$ 0.1 cm	Uc $\pm$ 0.1 cm/s
PC	h18_C1/C2/C3	/	4.7/7.8/10.1
PC	h27_C1/C2/C3	/	4.2/7.2/14.2
PC	h40_C1/C2/C3	/	4.6/7.6/12.7
PW	h18_f07_W1/W2/W3	1.0/1.6/2.3	0
PW	h27_f07_W1/W2/W3/W4/W5	1.0/1.6/2.3/3.0/4.1	0
PW	h36_f07_W1/W2/W3/W4/W5	1.0/1.6/2.3/3.0/4.2	0

PW	h40_f07_W1/W2/W3/W4/W5	1.0/1.5/2.3/3.0/4.1	0
PW	h45_f05_W1/W2/W3/W4/W5	0.9/1.5/2.1/3.0/4.0	0
PW	h45_f07_W1/W2/W3/W4/W5	1.0/1.5/2.2/2.9/4.0	0
PW	h45_f09_W1/W2/W3/W4/W5	0.9/1.5/2.2/3.1/4.1	0
CW	h18_f07_C1W1/W3	1.1/2.6	4.7
CW	h18_f07_C2W1/W3	1.0/2.5	7.8
CW	h27_f07_C1W1/W3/W4	1.0/2.3/3.1	4.2
CW	h27_f07_C2W1/W3/W4/W5	1.1/2.3/3.2	7.2
CW	h40_f07_C1W3/W4/W5	2.2/3.1/4.0	4.6
CW	h40_f07_C2W3/W4/W5	2.2/3.1/4.0	7.6

219

220 Two Nortek Vectrino+ were used to measure the vertical profiles of velocity with 1 to 2 cm  
 221 vertical resolution at P1 (upstream of the meadow) and P2 (within the meadow) (Fig. 1b). At each  
 222 measurement point, the Vectrino+ recorded a 1-min record with a sampling frequency of 200 Hz.  
 223 Upstream of the meadow velocity was measured at the channel centerline. Inside the meadow,  
 224 velocity measurements were made at one ( $y_2$  or  $y_4$  in Fig. 3b, as in Zhang et al., 2022, 2021) or  
 225 five lateral locations near the flume centerline (red pluses in Fig. 3b, as in Zhang and Nepf, 2021a).  
 226

### 227 2.3 Data analysis

228 The free surface displacement, force, and velocity data were processed in a similar fashion.  
 229 First, the analysis of wave data will be described in detail. The wave gauge has an accuracy of 0.2  
 230 (0.7) mm on average (maximum) based on the standard deviation of the raw data under still water  
 231 conditions. For each record, the mean surface position was removed from the time series to obtain  
 232 the free surface displacement data  $\eta$ . The surface displacement time series was separated into  
 233 phase bins following (Lei and Nepf, 2019b; Zhang and Nepf, 2021a). Specifically, for sampling  
 234 duration  $T$ , a wave measurement record contains  $M = \text{floor}(T/T_w)$  wave periods, with  $\text{floor}()$   
 235 denoting a downward rounding function. Each wave period contains  $\gamma = T_w f_s$  samples and thus  $\gamma$   
 236 phase bins.  $f_s$  is the sampling frequency. The phase-averaged free surface displacement in the  $n^{\text{th}}$   
 237 phase bin ( $n = 1$  to  $\text{floor}(\gamma)$ ), corresponding to phase  $\phi = 2\pi n/\gamma$ , was defined as,

$$238 \quad \tilde{\eta}(\phi(n)) = \frac{1}{M} \sum_{m=0}^{M-1} \eta(n + \gamma m) \quad (1)$$

239  $\tilde{\eta}$  denotes the phase-averaged value. Within each phase bin, the standard deviation of  $\tilde{\eta}$  was 0.7  
 240 (3.6) mm on average (maximum) based on the IE tests. Increasing current intensity led to higher

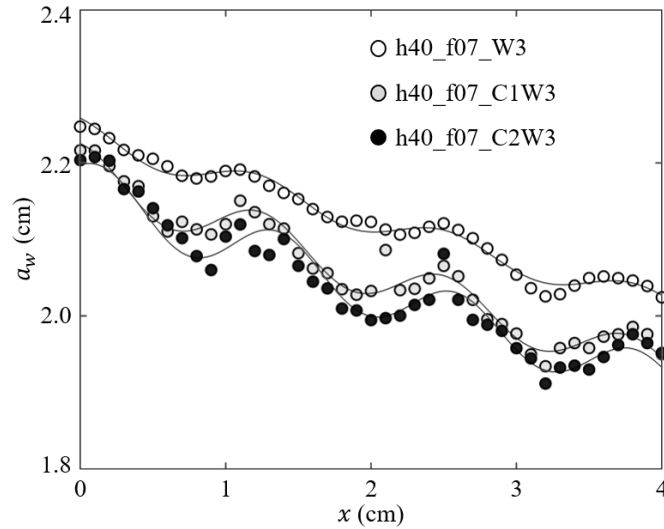
241 uncertainty in  $\check{\eta}$ . The wave amplitude  $a_w$  was calculated from the root-mean-square surface  
 242 displacement,

$$243 \quad a_w = \sqrt{\frac{2}{\gamma} \sum_{n=1}^{\gamma} \check{\eta}(\phi(n))^2} \quad (2)$$

244 For ME, the spatial evolution of wave amplitude can be used to estimate the wave damping  
 245 by vegetation. However, note that the wave amplitude reflected the sum of the incoming wave and  
 246 the beach-reflected wave, the superposition of which resulted in an amplitude modulation at an  
 247 interval of  $\lambda/2$  (with wavelength  $\lambda$ , e.g., Fig. 4). Accounting for the wave modulation, the wave  
 248 decay coefficient  $K_{Df}$  was estimated by fitting the measured amplitudes (Lei and Nepf, 2019b),

$$249 \quad \frac{1}{a_{w,x}} = K_{Df}x + C_1 \cos(2kx + \epsilon) + C_2 \quad (3)$$

250 in which  $k = 2\pi/\lambda$  is the wavenumber, and  $\epsilon$ ,  $C_1$ , and  $C_2$  are fitting parameters. Examples are  
 251 shown in Fig. 4. Wave decay attributed to the plants ( $K_D$  [ $m^{-2}$ ]) was obtained by subtracting the  
 252 decay coefficient obtained in the flume without plants.



253  
 254 **Fig. 4.** Measured wave amplitude (symbols) and the fitted Eq. 3 (curves) for h40\_f07\_W3,  
 255 h40\_f07\_C1W3, and h40\_f07\_C2W3 with the similar wave amplitude but increasing current.  
 256 (adapted from Figure 4 in Zhang and Nepf, 2021a)

257  
 258 For the individual plant experiments, a time lag of  $dt = 74 \pm 4$  ms (SD) was determined  
 259 between the force sensor and wave gauge due to the difference in the instruments' reaction time.  
 260 This time lag was accounted for by removing the free surface displacement records (about 148  
 261 data points) before the first force sensor record. The FFT (fast Fourier transform) function in

262 MATLAB was used to filter out high-frequency noise (frequency components greater than 2 Hz),  
 263 which was negligible based on the frequency spectrum and was subtracted from the raw data. The  
 264 plant force time series,  $F$ , was obtained by removing the offset measured with still water conditions.  
 265 The phase-averaged plant drag,  $\check{F}$ , was obtained in similar way as Eq. 1. The maximum, minimum,  
 266 and mean value of  $\check{F}$  are reported as  $F_{max}$ ,  $F_{min}$ , and  $F_m$ , respectively. For pure current conditions,  
 267  $F_m$ , was defined by the average over the 3-minute record.

268 Based on the standard deviation among ten still water measurements, considering different  
 269 water depth and different plants installed on the force sensor, the accuracy of the force  
 270 measurements was determined to be 0.001 N (0.002 N) average (maximum). The force exerted on  
 271 the post alone (without plant) was less than 3% of the force on the model plant (Zhang and Nepf,  
 272 2021b, 2022). Consequently, in this dataset, the force due to the post was neglected and not  
 273 subtracted from the measurements. However, note that the force on the post can contribute up to  
 274 30% of the total force measured for an individual leaf. Hence, when using the leaf force data, it  
 275 may be necessary to exclude the force due to the post.

276 For all velocity data, two despiking methods were applied to identify abnormal data points,  
 277 which were replaced by a NAN (not a number) value. First, data points were identified if the  
 278 associated acceleration exceeded the gravitational acceleration. Second, a threshold,  $\pm 3\sigma$  with  $\sigma$   
 279 the standard deviation, was applied to identify abnormal data within each phase bins for conditions  
 280 with waves and in the whole time series for the pure current cases (Zhang and Nepf, 2022). The  
 281 despiked velocity data is denoted  $u$ ,  $v$ ,  $w$ , respectively, for the longitudinal, lateral, and vertical  
 282 directions. For the horizontal velocity component, the velocity data was separated into a phase  
 283 averaged value  $\check{u}(\phi)$  and a turbulent velocity fluctuation  $u'$ ,

$$284 \quad u = \check{u}(\phi) + u' = u_m + \check{u}_w(\phi) + u' \quad (4)$$

285  $\check{u}(\phi)$  was calculated in the same manner as Eq. 1, and then further separated into a time mean  
 286 velocity  $u_m = \frac{1}{2\pi} \int_0^{2\pi} \check{u}(\phi) d\phi$  and a wave orbital velocity  $\check{u}_w(\phi) = \check{u}(\phi) - u_m$ . The magnitude of  
 287 wave orbital velocity was defined as

$$288 \quad u_w = \sqrt{2 \frac{1}{2\pi} \int_0^{2\pi} (\check{u}_w(\phi))^2 d\phi} \quad (5)$$

289 The root mean square of the fluctuating velocity component within each phase bin (e.g.,

$$290 \quad u_{rms} = \sqrt{\frac{1}{n} \sum_1^n u'^2}) \text{ was used to estimate the turbulent kinetic energy in that phase bin, } tke(\phi) =$$

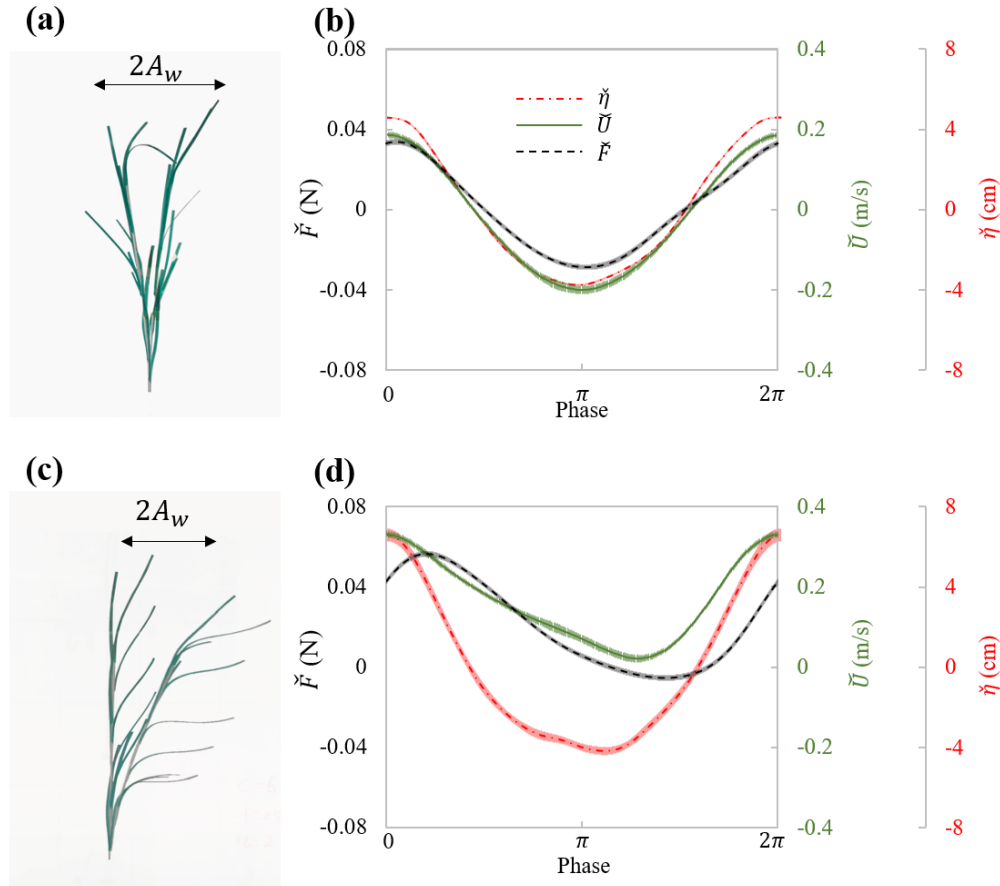
291  $(u_{rms}^2 + v_{rms}^2 + w_{rms}^2)/2$ . The time-average turbulent kinetic energy, TKE, was defined as the  
 292 average of  $tke(\phi)$  over all phases. The depth- and phase-averaged horizontal velocity was defined  
 293 as  $\bar{U} = \frac{1}{h} \int_0^h \bar{u}(\phi, z) dz$ . The depth-average velocity statistics reported for each velocity profile  
 294 includes the maximum  $U_{max}$ , minimum  $U_{min}$ , and mean  $U_m$  value of  $\bar{U}$ . The depth-average wave  
 295 orbital velocity was defined as  $U_w = \sqrt{2 \frac{1}{2\pi} \int_0^{2\pi} (\bar{U} - U_m)^2 d\phi}$ . For pure current cases,  $U_m = U_c$   
 296 was defined by the depth- and time-averaged velocity over all measurements. The phase-averaged  
 297 and depth-averaged values for the lateral ( $v$ ) and vertical ( $w$ ) velocity components were calculated  
 298 in the same way as the horizontal component.

299

### 300 **3. Data**

#### 301 **3.1 Data for the individual plant experiments (IE)**

302 In experiments with individual plants, the plant force and free surface displacement at the  
 303 same streamwise ( $x$ ) location as the plant were measured simultaneously. The motion of the plant  
 304 was captured in videos during the force measurement. The flow velocity was measured separately,  
 305 but assumed to be in-phase with the free surface displacement. These data contained all relevant  
 306 parameters necessary for understanding the hydrodynamic performance of an individual marsh  
 307 plant. For example, Fig. 5 shows the maximum plant motion, phase-averaged plant drag and free  
 308 surface displacement, as well as the phase- and depth-averaged velocity for the model plant under  
 309 the same wave with and without following current. These data demonstrate a strong dependence  
 310 of plant force on the instantaneous flow velocity, which can be utilized to validate predictions of  
 311 plant drag, as in Zhang and Nepf (2022, 2021b). It is worth noting that the phase-averaged data  
 312 allows for detailed validation of phase resolving models. Only a few studies, e.g., Jacobsen et al.  
 313 (2019); Luhar and Nepf (2016), have reported time-varying velocity and force on flexible plants.  
 314 However, for modeling and validating plant motion and time-varying plant force, high-resolution  
 315 time-varying horizontal and vertical velocity are required. For example, Zhu et al. (2020)  
 316 demonstrated that the vertical velocity results in asymmetric plant motion, even when subjected to  
 317 symmetric waves. For high resolution model validation, the present dataset includes both the time-  
 318 varying horizontal and vertical velocity, as well as the synchronized force and free surface  
 319 displacement for both live and model plants.

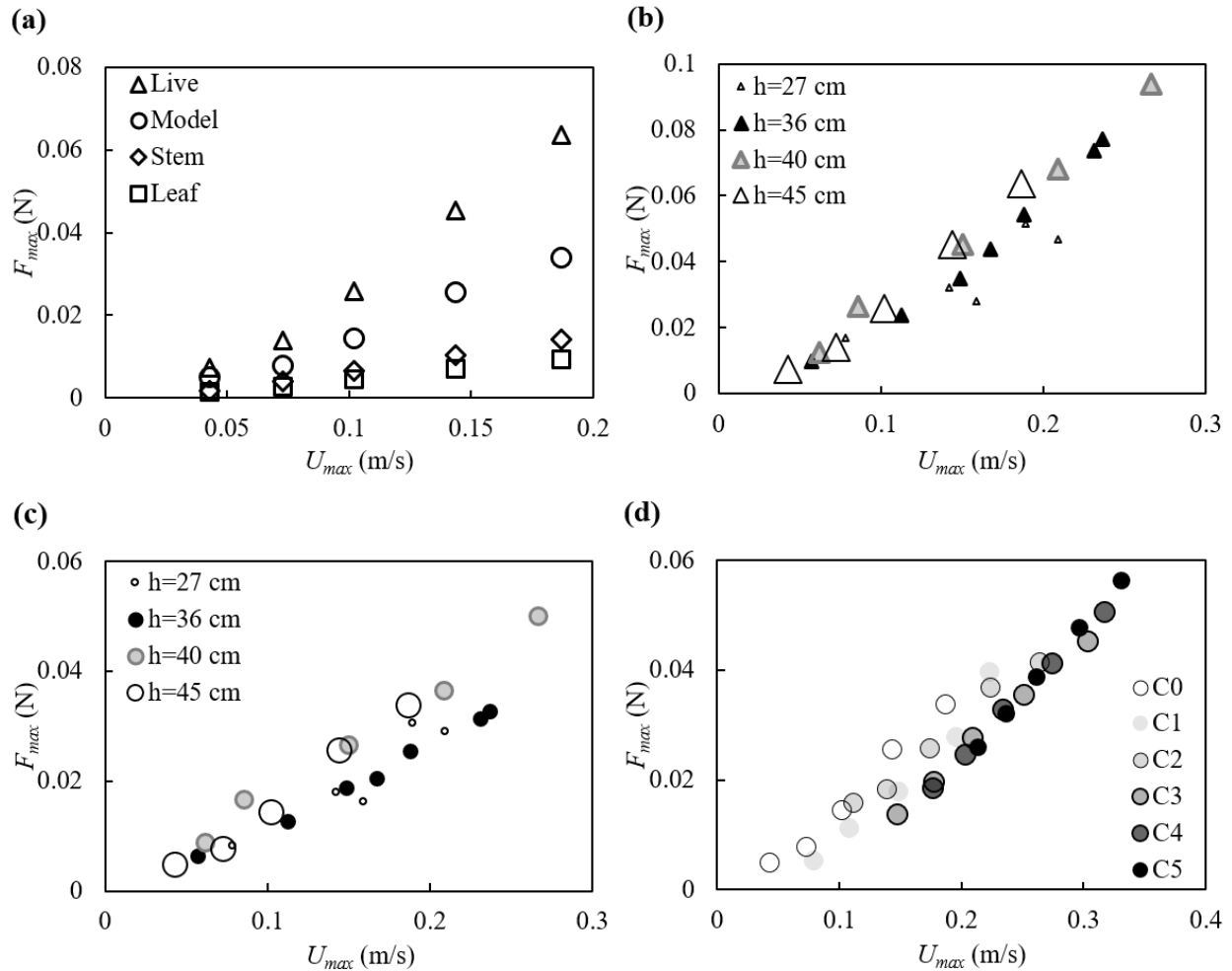


320  
 321 **Fig. 5** Plant motion and phase-averaged measurements of force (black curve), surface  
 322 displacement (red curve) and velocity (green curve) for (a) and (b) model\_h45\_f05\_W5 ( $U_m = -$   
 323  $1.9$  cm/s, and  $U_w = 19.1$  cm/s); and (c) and (d) model\_h45\_f05\_C5W5 ( $U_m = -16.3$  cm/s, and  $U_w$   
 324  $= 14.3$  cm/s). (a) and (c) showed the digital image of model plant at the maximum downstream  
 325 and upstream posture within the wave cycle. The thin shading in each curve in subplots (b) and (d)  
 326 indicate the uncertainty in each phase. (modified based on figure 5 in Zhang and Nepf, 2022).

327  
 328 The force measurements suggested that the force on the full plant was smaller than the sum of  
 329 forces on all the leaves and stem acting alone, suggesting that sheltering and interaction among the  
 330 leaves and stem decreased the force exerted on the full plant compared to the leaves and stem in  
 331 isolation (Fig. 6a). The decrease in plant drag can be represented by a constant sheltering  
 332 coefficient  $C_s$  for a given plant morphology. Specifically, for a plant with  $N_l$  leaves attached to a  
 333 central stem, the force of on the full plant is:  $F(\text{plant}) = C_s \times F(\text{one leaf}) \times N_l + F(\text{stem})$ , with  $C_s$   
 334  $= 0.6$  for the model plant reported here (Zhang and Nepf, 2021b). The leaves was estimated to

335 contributed  $72\% \pm 1\%$  of the plant-scale drag (Zhang and Nepf, 2021b). With this finding, the  
336 hydrodynamic force on a plant with complex leaf and stem morphology can be easily estimated  
337 using the force prediction for an individual simple structure (a flat leaf or a cylindrical stem, e.g.,  
338 the models described in Zhu et al., 2020; Mullarney and Henderson, 2010; Luhar and Nepf, 2011,  
339 2016)).

340 The maximum force on the plant is plotted against the maximum depth- and phase-averaged  
341 velocity in Fig. 6. Note that for  $h = 40$  and  $45$  cm, both the live and model plant were submerged  
342 at the wave crest (see videos in <https://doi.org/10.6084/m9.figshare.24117324>). The maximum  
343 force for these two water depths followed the same trend with velocity (Fig. 6b and c). For smaller  
344 water depth, only part of the plant was submerged, such that the plant felt smaller force under  
345 similar horizontal velocity (Fig. 6b and c). The relationship between  $F_{max}$  and  $U_{max}$  was similar for  
346 different current velocity, but curves were shifted to the right as current increased (darker symbols  
347 in Fig. 6d), i.e., as current magnitude increased, a greater  $U_{max}$  was needed to reach the same  $F_{max}$   
348 (Fig. 6 d).



349  
 350 **Fig. 6** maximum force on the plant plotted against the maximum horizontal velocity for (a) all  
 351 plants at  $h = 45$  cm, (b) the live plant and (c) the model plant under pure waves, (d) the model plant  
 352 at  $h = 45$  cm under combined current and waves with increasing current intensity labeled by C0 to  
 353 C5. All the cases shown are associated with wave frequency  $f = 0.5$  Hz. The uncertainty in the  
 354 force measurements, not shown in the figures, ranged from 0.001 to 0.002 N based on the standard  
 355 deviations of force in each wave phase.

356

### 357 3.2 Canopy velocity structure and turbulence

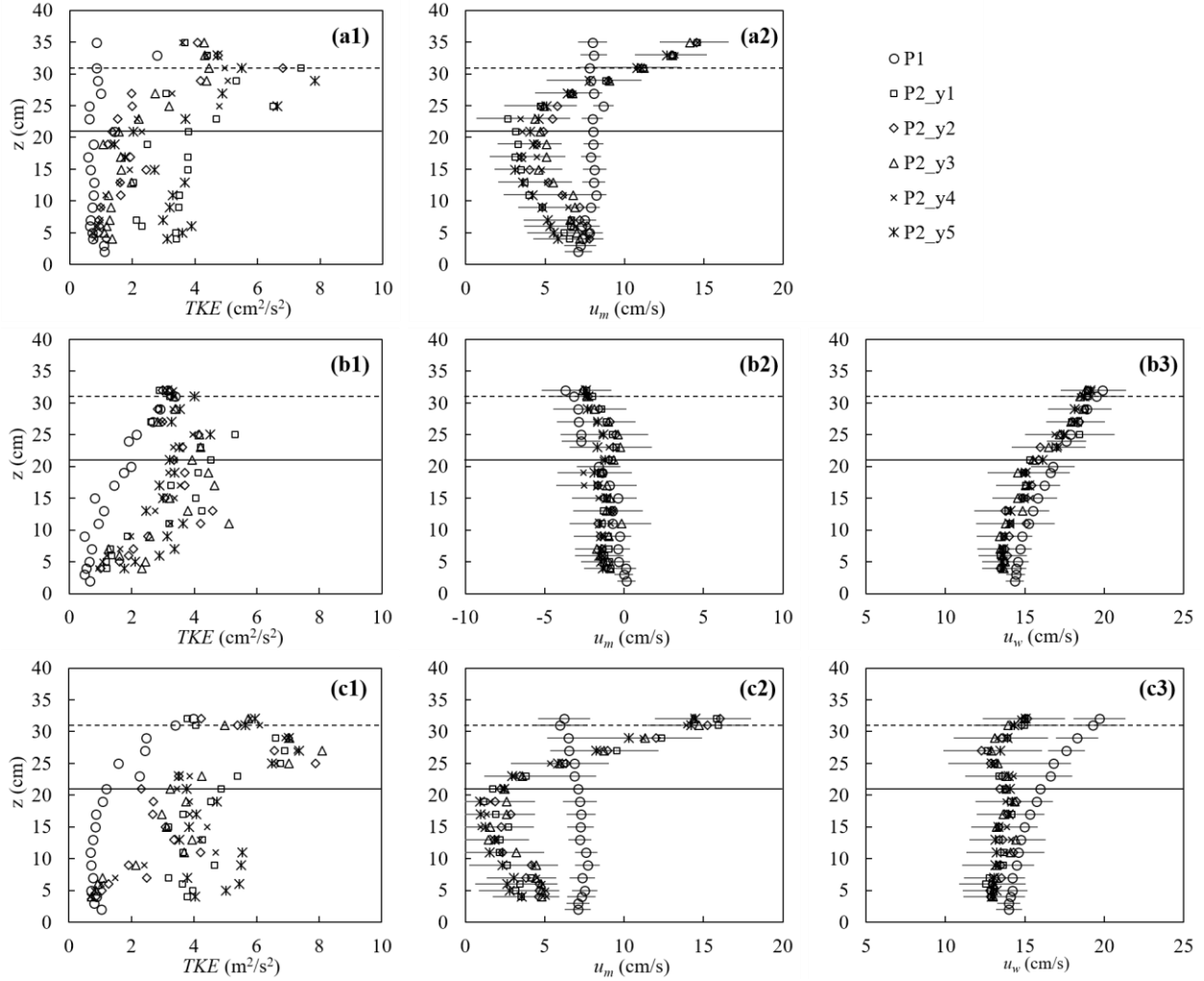
358 The canopy velocity structure and turbulence were altered by the plant drag, which in turn  
 359 affected the dissipation of wave energy. Fig. 7 shows a few examples of the turbulence and velocity  
 360 structure of the ME test. First, for pure current, the presence of the canopy significantly modified  
 361 both the flow structure and turbulent intensity (Fig. 7a). The time-mean velocity  $u_m$  at P1 (2 m  
 362 upstream of the meadow) exhibited a boundary-layer velocity profile (circles in Fig. 7a2), and the



363 TKE was essentially uniform, with a slight increase near the bed (circles in Fig. 7a1). The canopy  
364 resistance reduced  $u_m$  within the canopy height by a factor of 0.29 and redirected the time-mean  
365 flow above the canopy, forming a shear layer extending from the top of the stems toward the free  
366 surface (Fig. 7a2). Within the canopy, the magnitude of the horizontal velocity was negatively  
367 correlated with the distribution of plant frontal area (Nepf, 2012). Specifically, a greater time-mean  
368 velocity was observed near the bed (Fig. 7a2) where the plant frontal area was smaller (Fig. 2b).  
369 Considering that the velocity is zero at the bed, the velocity profile  $u_m$  exhibited an “S” shape at  
370 P2 (2.46 m inside the meadow). The time-mean velocity  $u_m$  at five lateral locations within the  
371 canopy (y1 to y5, red pluses in Fig. 3b) were the same within uncertainty, but the TKE was  
372 maximum directly upstream of a plant (P2\_y1 and P2\_y5) and minimum directly downstream of  
373 a plant (P2\_y3). The maximum TKE was observed near the top of the canopy due to shear  
374 production associated with the strong vertical gradient in velocity (Fig. 7a2).

375 For pure waves, the turbulence intensity was maximum near the free surface and decreased  
376 with distance from the surface at P1 (circles in Fig. 7b1). Note that the time-mean velocity can be  
377 slightly negative in a closed flume, reflecting the return current that develops to balance the mass  
378 transport associated with the Stokes draft (Monismith, 2020), and its magnitude increases with  
379 distance from the bottom (Fig. 7b2). The presence of the canopy reduced the wave orbital velocity  
380  $u_w$  slightly due to the wave energy dissipation by the plants (Fig. 7b3) and adjusted the time-mean  
381 velocity to a more uniform profile (Fig. 7b2). Compared to TKE measured at P1, the turbulent  
382 intensity at P2 was larger within the canopy, but similar near the top of the canopy (Fig. 7b1).  
383 Specifically, above the canopy height, TKE was primarily generated by the mean shear production,  
384 and the similar TKE at P1 and P2 can be explained by the comparable time-mean velocity profiles,  
385 i.e., comparable shear. Within the canopy, TKE was mainly generated by the plant form drag, such  
386 that TKE was obviously larger compared to P1.

387



388

389 **Fig. 7** The turbulent kinetic energy (left), horizontal time-mean velocity (middle), and wave orbital  
 390 velocity (right column) for (a) pure current (h40\_C2,  $U_m = 7.7$  cm/s), (b) pure waves  
 391 (h40\_f07\_W5,  $U_m = -1.8$  cm/s,  $U_w = 16.7$  cm/s), and (c) combined current and waves  
 392 (h40\_f07\_C2W5,  $U_m = 7.0$  cm/s,  $U_w = 15.6$  cm/s). For the cases shown, water depth  $h = 40$  cm.  
 393 The measurements were made at P1 (2 m in front of the meadow at flume central) and P2 (2.46 m  
 394 in the meadow) at five lateral positions y1 to y5 shown as red plus signs in Fig. 3b. The horizontal  
 395 bars indicate the average standard deviation within each phase bins. The solid and dashed  
 396 horizontal lines indicate the stem height and erect canopy height, respectively.

397

398 Finally, consider the conditions with combined current and waves (Fig. 7c). Upstream of the  
 399 canopy (position P1, open circles in Fig. 7), the time-mean velocity  $u_m$  (Fig. 7c2) and wave  
 400 velocity  $u_w$  (Fig. 7c3) exhibited the same vertical profile shape as that observed for the pure

401 current (Fig. 7a2) and pure wave conditions (Fig. 7b3), respectively, and TKE (Fig. 7c1) was  
402 similar in magnitude to the pure wave condition (Fig. 7b1). This might be explained by time-mean  
403 velocity gradients (Fig. 7c2 and 7b2), which feed shear-production of turbulence and are similar  
404 in pure wave and combined wave-current conditions. Within the meadow (P2), adding current  
405 resulted in greater decrease in  $u_w$  and a more uniform profile (Fig. 7c3), compared to that under  
406 pure waves (Fig. 7b3). Smaller in-canopy wave orbital velocity was explained by greater plant  
407 drag (positively related to  $u_m + u_w$  as in Fig. 6) and hence greater wave energy dissipation under  
408 combined conditions than the same pure wave (Zhang and Nepf, 2021a). Similarly, stronger plant  
409 resistance under combined current and waves resulted in a greater reduction in time-mean velocity  
410 within the canopy, relative to upstream, compared to pure current conditions (Fig. 7c2).  
411 Specifically, for the combined wave-current conditions,  $u_m$  within the canopy (roughly  $z < 30$  cm)  
412 at P2 was reduced by a factor of 0.42, compared to  $u_m$  at P1. Whereas for the pure current  
413 condition the reduction was only a factor of 0.29. Finally, in combined wave-current conditions,  
414 the TKE within the meadow (P2) was greater than TKE for either the pure current or pure wave  
415 conditions (comparing the left column in Fig. 7). This was consistent with the greater reduction in  
416 in-canopy current and greater dissipation of wave energy, because energy lost from time-mean and  
417 wave energy is converted into turbulent kinetic energy. In addition, in the combined wave-current  
418 conditions two regions of high TKE were observed, one near the top of the canopy, associated  
419 with shear-generated turbulence and consisted with the pure current condition, and a second within  
420 the lower canopy, associated with plant element-generated turbulence (Fig. 7c1).

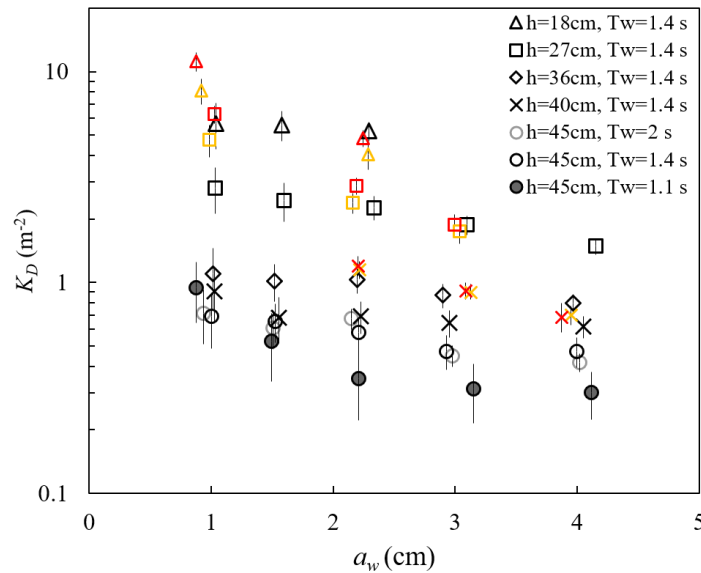
421 In addition to the time-mean velocity, wave-orbital velocity, and turbulent kinetic energy, the  
422 time series for each velocity component ( $u, v, w$ ) as both raw data and phase-averaged velocity for  
423 all ME are contained in the dataset. This dataset can be used to describe the physical mechanisms  
424 associated with current-wave-vegetation interaction.

425

### 426 **3.3 Wave decay over salt marsh meadow**

427 ME measured the free surface displacement at 2000 Hz, with a spatial interval of 10 or 15 cm  
428 along the meadow length. These data can be used to examine the wave amplitude dissipation (as  
429 in Zhang et al., 2021, 2022; Zhang and Nepf, 2021a) and wave shape transformation over a salt  
430 marsh meadow. The wave decay coefficient,  $K_D$ , increased with decreasing water depth and  
431 decreasing wave amplitude (Fig. 8). For a constant water depth (circles in Fig. 8), as wave period

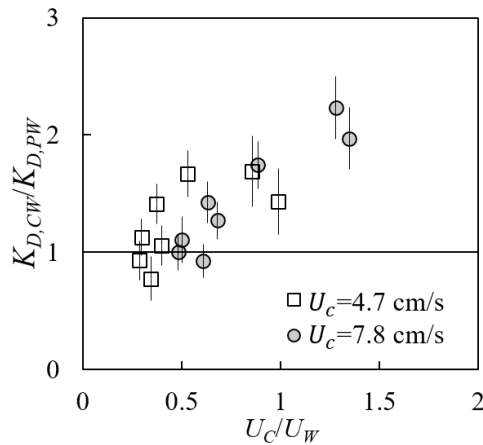
432 increased from  $T_w = 1.12$  s to 1.44,  $K_D$  increased, but then remained the same within uncertainty  
 433 between  $T_w = 1.44$  and 2.01 s. The dependence of  $K_D$  on water depth, wave amplitude, and wave  
 434 period can be explained by how these parameters affect the fluid velocity and drag on the plant.  
 435 First, for the same  $a_w$  and  $T_w$ ,  $U_w$  increases with decreasing  $h$ , generating greater plant drag and  
 436 thus greater wave energy dissipation as water depth decreases. Second, for a constant depth ( $h =$   
 437 45 cm) and wave amplitude, an increase in wave period (here,  $T_w = 1.11, 1.44,$  and 2.01 s) produces  
 438 a decrease in dimensionless wave number  $kh = 1.55, 1.08,$  and 0.77, respectively. This decrease in  
 439  $kh$  is associated with wave velocity profile that is increasingly more uniform, producing larger  
 440 depth-averaged velocity magnitude (see Figure B.1 in Zhang et al., 2022). Finally, with constant  
 441 depth and wave period, an increase in wave amplitude results in greater plant motion within the  
 442 wave cycle, which leads to a greater reduction in the plant drag (due to greater plant  
 443 reconfiguration) and wave dissipation. Detailed mechanisms and scaling analysis was provided in  
 444 Zhang et al. (2022).



445  
 446 **Fig. 8** Wave decay coefficients  $K_D$  for all cases reported in the (Zhang and Nepf, 2021a; Zhang et  
 447 al., 2021, 2022). The yellow and red symbols indicated waves with small ( $U_c = 4.7$  cm/s) and  
 448 larger ( $U_c = 7.8$  cm/s) following current, respectively. The vertical bars indicate uncertainty in  $K_D$ .  
 449 (adopted from Figure 4a in Zhang et al., 2021)

450  
 451 Adding a following current tended to increase wave dissipation. For the same water depth and  
 452 wave period,  $K_D$  increased with increasing current magnitude (red and yellow symbols in Fig. 8),

453 compared to pure wave conditions (black symbols in Fig. 8) with similar wave amplitude. The  
 454 effect of a following current increasing wave dissipation is shown more clearly in Fig. 9, which  
 455 shows the ratio of wave decay coefficient in combined current and wave ( $K_{D,cw}$ ) normalized by  
 456 the value in pure waves ( $K_{D,pw}$ ). Generally, as current increased,  $K_{D,cw}/K_{D,pw}$  increased above 1.  
 457 There were a few exceptions for  $U_c/U_w < 0.6$ , for which adding a weak current slightly reduced  
 458 the wave decay coefficient, i.e.,  $K_{D,cw}/K_{D,pw} < 1$ . This opposite effect of current on wave decay  
 459 has been reported in a few previous studies (Hu et al., 2014; Li and Yan, 2007; Yin et al., 2020;  
 460 Paul et al., 2012; Losada et al., 2016; Zhao et al., 2020). Paul et al. (2012) attributed the reduction  
 461 in wave dissipation with current mainly to an observed reduction in plant motion. However, for  
 462 rigid canopies, following current was also observed to reduce wave dissipation when  $U_c/U_w$  was  
 463 smaller than a transition value of 0.65 to 1.25 (Hu et al., 2014) and 0.37 to 1.54 (Yin et al., 2020),  
 464 but larger currents increased wave dissipation above pure wave values ( $K_{D,cw}/K_{D,pw} > 1$ , Hu et  
 465 al., 2014; Li and Yan, 2007; Yin et al., 2020). With an opposing current, wave dissipation was  
 466 enhanced and to a higher degree compared to that of the following current of similar magnitude  
 467 (Hu et al., 2021).



468  
 469 **Fig. 9** Ratio of wave decay coefficients under combined condition to pure wave condition plotted  
 470 against the ratio of current to wave velocity. (adopted from Figure 6a in Zhang and Nepf, 2021a)  
 471

472 Based on our laboratory measurements and theoretical analysis, we explained the different  
 473 observed effects of current on wave dissipation as the result of the following competing  
 474 mechanisms. First, consider that the wave energy was only dissipated by plants, the time rate of  
 475 energy dissipation scales with plant drag and canopy total velocity  $E_D \sim F_D U$ . Adding current

476 increases the total fluid velocity (Fig. 7) and thus the total plant force (Fig. 6), resulting in a greater  
477 wave energy dissipation, compared to the same pure wave. Second, the influence of current on  
478 wave dissipation is further modulated by the effect of plant resistance on the time-mean canopy  
479 flow structure (Fig. 7). In particular, the time-mean velocity within the canopy is significantly  
480 reduced compared to velocity upstream of the canopy at the same distance from the bed (P1 in Fig.  
481 7). A reduction in time-mean velocity in the canopy, relative to the depth-averaged, time-mean  
482 velocity, decreases the impact of current on wave decay. Because the in-canopy current has a  
483 greater reduction for a denser canopy, the influence of current on wave decay is diminished for a  
484 denser canopy, relative to a sparser canopy. Third, current changes the speed of wave energy  
485 propagation, i.e., the wave group velocity  $C_g = C_{g,pw} + U_c$ , which connects the time-rate of wave  
486 energy dissipation to the spatial rate of wave energy dissipation (represented by  $K_D$ ). For the same  
487  $|U_c|$  and plant drag (associated with the same  $E_D$ ), an opposing (following) current decreases  
488 (increases)  $C_g$  and generates larger (smaller)  $K_D$  (spatial rate of amplitude decay).

489 For the experiments describe here, conducted in a finite length channel, the time-mean  
490 velocity was slightly negative for pure waves (Fig. 7b2), such that adding small following current  
491 could lead to a decrease in the magnitude of time-mean velocity. Further increase in the current  
492 magnitude would increase the magnitude of time-mean and total velocity, which is why the present  
493 and previous studies (Hu et al., 2014; Yin et al., 2020) observed a reduction in  $K_D$  only under small  
494 following current, with a larger following current increasing  $K_D$ , compared to the same pure wave.  
495 The greater increase in  $K_D$  under an opposing current than under a following current with the same  
496 magnitude, as observed in (Hu et al., 2014; Yin et al., 2020), can be explained by the effect of  
497 current direction on wave group velocity (the third mechanism above). The decrease in  $K_D$   
498 observed in highly flexible seagrass mimics (Paul et al., 2012) under following current might be  
499 explained by the weaker increase in plant drag and canopy flow velocity (associated with limited  
500 increase in the time-rate energy dissipation), and the decrease in  $K_D$  due to an increase in wave  
501 group velocity  $C_g$  (the third mechanism above), compared to pure wave conditions. Specifically,  
502 increasing current led to a more pronated plant posture and decreased force on the flexible leaves,  
503 compared to a leaf under the same pure wave (see Figure 6 and table 1 in Lei and Nepf, 2019a).  
504 Further, the time-mean velocity within the canopy height was smaller under combined current and  
505 waves than for pure current of the same magnitude (see Fig. 7a2 and 7c2), and the canopy time-  
506 mean velocity was further reduced by the decrease in canopy height due to plant reconfiguration,

507 both because the deflection increased the plant solid volume fraction within the canopy, and  
508 because in-canopy velocity decreases with increasing degree of canopy submergence (Chen et al.,  
509 2013).

510

#### 511 **4. Data availability**

512 All instrument measured data presented in this paper are available from Figshare  
513 (<https://doi.org/10.6084/m9.figshare.24117144>; Zhang and Nepf, 2023a). The repository includes  
514 the raw time series, phase-averaged, and various statistical metrics (time-mean, maximum,  
515 minimum) of force, surface displacement, and velocity. A “readme.pdf” file included in the  
516 repository provides additional data instructions. To enhance the accessibility of the data, we  
517 prepared the data in two formats, i.e., the SMCW.mat file and the SMCW.nc file, both of which  
518 were included in the Figshare link. The SMCW.mat can be directly imported into MATLAB and  
519 Python. The SMCW.nc file is a NetCDF file with metadata that can be accessed by C, C++, Fortran,  
520 Python as well as Matlab. The plant motion recorded in the individual plant experiments can be  
521 found at: <https://doi.org/10.6084/m9.figshare.24117324>; Zhang and Nepf, 2023b. For each plant,  
522 a video with the same frame but including a ruler was included to give a scale of the plant motion.

523

#### 524 **5. Recommendations for data reuse**

##### 525 **5.1 Plant dynamic model validation**

526 The plant motion videos, phase-resolving plant drag, free surface displacement, and 3D  
527 velocity data can be used to validate phase-resolving plant dynamic models. The time-averaged  
528 force and velocity statistics can be used to validate phase-averaged plant drag models (as in Zhang  
529 and Nepf, 2021b, 2022). This dataset includes data not included in Zhang and Nepf (2021 and  
530 2022) which is associated with strongly nonlinear waves, which reveal the nonlinear effects on  
531 plant motion and drag.

532 The measurements captured a phase lag between the plant force and wave motion (reflected  
533 by the free surface displacement). The presence of a following current tended to increase the  
534 magnitude of this phase lag (Fig. 5). The dataset in Hu et al. (2021) also contained time lags  
535 between the wave (velocity) and force data (Figure 5 in their paper). However, their wave and  
536 force data were not measured simultaneously, so the source of phase lag was unclear. Using a high-  
537 resolution synchronization method, Jacobsen et al. (2019) were able to capture the phase lag

538 between the motion of a single flexible leaf and the fluid velocity, which informed an important  
539 knowledge gap in describing the physical cause of the observed phase lag. The present dataset can  
540 be used to deepen our understanding of the plant motion and force in response to waves with and  
541 without current in high temporal resolution.

542

## 543 **5.2 Flow structure within salt marsh meadow**

544 The drag associated with a canopy has long been known to modify the vertical structure of  
545 current and wave velocity (Chen et al., 2013; Lowe et al., 2005; Zeller et al., 2015; Lei and Nepf,  
546 2021), but few data have been reported under combined current and waves. The present dataset  
547 directly compares the flow structure within a marsh canopy under pure current, pure wave, and  
548 their combination. Lowe et al. (2005) showed that a submerged canopy is more effective in  
549 reducing the time-mean velocity than the wave orbital velocity. They developed a 2-layer model  
550 to predict the canopy wave orbital velocity without considering the influence of current. Zeller et  
551 al. (2015) developed a prediction for the canopy total velocity under combined current and waves.  
552 However, their model was only validated using five flow conditions in a rigid canopy. Further,  
553 previous studies of canopy velocity structure seldom compare the reduction of time-mean and  
554 wave orbital velocity using laboratory data measured under current and waves acting alone and in  
555 combination. The present ME dataset provides high resolution velocity profiles upstream (single  
556 profile) and within (five lateral locations) a meadow under combined current and wave conditions  
557 (e.g., Fig. 7). The dataset covers water depth to plant height ratios from emergent to submerged  
558 and velocity ratios  $U_c/U_w = 0.16$  to 4.7. Measurements were also made using the same current  
559 and wave acting alone. This dataset can be utilized to study the interaction between current and  
560 waves. In particular, the canopy time-mean velocity was reduced when waves were present (Fig.  
561 7b2 and c2), suggesting that the waves enhanced the time-mean plant drag. The dataset can be  
562 used to validate theoretical and numerical models that predict canopy current and wave velocity.

## 563 **5.3 Turbulent kinetic energy due to salt marsh**

564 As shown in Fig.7 and described in section 3.2, the presence of marsh plants significantly  
565 enhanced turbulence intensity. For current over bare beds, turbulence is generated by spatial  
566 gradients in time-mean velocity (shear production), and the TKE is essentially uniform, except  
567 very close to the bed (circles in Fig. 7a1). However, when waves are presented, TKE was  
568 maximum near free surface and decreased away from the surface (circles in Fig. 7b1 and c1),



569 possibly due to time-mean shear introduced by the return current associated with wave conditions  
570 (circles in Fig. 7b3 and c3). Within the meadow, the TKE varied with position relative to individual  
571 plants. TKE was largest under combined current and wave conditions (compare the left column in  
572 Fig. 7), with turbulence peaks observed near the top of the canopy, associated with shear-  
573 production by the time-mean current, and also within the canopy, associated with turbulence  
574 production in the wakes of individual plants (Fig. 7c1). This dataset can be used to develop and  
575 validate models to predict canopy turbulence (e.g., Xu and Nepf, 2020) and for use in numerical  
576 models (e.g., Tang and Lin, 2021).

#### 577 **5.4 Wave decay over salt marsh meadow**

578 The meadow experiments (ME) measured the free surface displacement along the length of  
579 the meadow with a horizontal interval of 10 and 15 cm, which included 18 to 26 points within one  
580 wave length (see Figure C.1 in Zhang et al., 2022). The raw time-series data can be utilized to  
581 analyze the transformation of wave shape, including wave skewness and wave asymmetry, over  
582 salt marshes. The wave shape is a crucial parameter when describing wave-driven sediment motion  
583 and hence important for the study of coast stability within salt marsh regions.

584 The wave dissipation dataset presented here adds to the dataset reported in Hu et al. (2021),  
585 expanding the range of conditions. Specifically, Hu et al. (2021) reported wave decay data over  
586 rigid cylinders, while the present dataset provides wave decay over model plants with more  
587 realistic morphology and flexibility. The dataset can be applied to validate phase-averaged (e.g.,  
588 Garzon et al., 2019a; Smith et al., 2016) and phase-resolving coastal models (e.g., Chen and Zou,  
589 2019; Mattis et al., 2019) in predicting the wave energy reduction by salt marshes.

590

591 **Author contributions.** XXZ designed the experiments, conducted the experiments and  
592 collected the raw data. XXZ prepared the manuscript, HN reviewed and edited the manuscript.

593 **Competing interests.** The contact author has declared that neither they nor their coauthors  
594 have any competing interests.

595 **Acknowledgments.** We thank Dr. Jiarui Lei for his guidance with the experimental equipment.

596 **Financial support.** This study was supported by the National Key Research and Development  
597 Program of China (No. 2022YFE0136700). Xiaoxia Zhang was supported by the China

598 Scholarship Council. The project also received support from the US National Science Foundation  
599 under EAR 1659923.

600

## 601 **6. References**

602 Barbier, E. B., Hacker, S. D., Kennedy, C., Koch, E. W., Stier, A. C., and Silliman, B. R.: The value of  
603 estuarine and coastal ecosystem services, *Ecological Monographs*, 81, 169–193,  
604 <https://doi.org/10.1890/10-1510.1>, 2011.

605 Boesch, D. F. and Turner, R. E.: Dependence of fishery species on salt marshes: The role of food and refuge,  
606 *Estuaries*, 7, 460–468, <https://doi.org/10.2307/1351627>, 1984.

607 Borges, F. O., Santos, C. P., Paula, J. R., Mateos-Naranjo, E., Redondo-Gomez, S., Adams, J. B., Caçador,  
608 I., Fonseca, V. F., Reis-Santos, P., Duarte, B., and Rosa, R.: Invasion and Extirpation Potential of Native  
609 and Invasive *Spartina* Species Under Climate Change, *Front. Mar. Sci.*, 8, 696333,  
610 <https://doi.org/10.3389/fmars.2021.696333>, 2021.

611 Chen, H. and Zou, Q.: Eulerian–Lagrangian flow-vegetation interaction model using immersed boundary  
612 method and OpenFOAM, *Advances in Water Resources*, 126, 176–192,  
613 <https://doi.org/10.1016/j.advwatres.2019.02.006>, 2019.

614 Chen, Z., Jiang, C., and Nepf, H.: Flow adjustment at the leading edge of a submerged aquatic canopy,  
615 *Water Resour. Res.*, 49, 5537–5551, <https://doi.org/10.1002/wrcr.20403>, 2013.

616 Elschot, K., Bouma, T. J., Temmerman, S., and Bakker, J. P.: Effects of long-term grazing on sediment  
617 deposition and salt-marsh accretion rates, *Estuarine, Coastal and Shelf Science*, 133, 109–115,  
618 <https://doi.org/10.1016/j.ecss.2013.08.021>, 2013.

619 Garzon, J. L., Miesse, T., and Ferreira, C. M.: Field-based numerical model investigation of wave  
620 propagation across marshes in the Chesapeake Bay under storm conditions, *Coastal Engineering*, 146,  
621 32–46, <https://doi.org/10.1016/j.coastaleng.2018.11.001>, 2019a.

622 Garzon, J. L., Maza, M., Ferreira, C. M., Lara, J. L., and Losada, I. J.: Wave attenuation by *Spartina*  
623 saltmarshes in the Chesapeake Bay under storm surge conditions, *J. Geophys. Res. Oceans*, 124, 5220–  
624 5243, <https://doi.org/10.1029/2018JC014865>, 2019b.

625 Gosselin, F., De Langre, E., and Machado-Almeida, B. A.: Drag reduction of flexible plates by  
626 reconfiguration, *J. Fluid Mech.*, 650, 319–341, <https://doi.org/10.1017/S0022112009993673>, 2010.

627 Harder, D. L., Speck, O., Hurd, C. L., and Speck, T.: Reconfiguration as a prerequisite for survival in highly  
628 unstable flow-dominated habitats, *J Plant Growth Regul*, 23, 98–107, <https://doi.org/10.1007/s00344-004-0043-1>, 2004.

630 Hu, Z., Suzuki, T., Zitman, T., Uittewaal, W., and Stive, M.: Laboratory study on wave dissipation by  
631 vegetation in combined current–wave flow, *Coastal Engineering*, 88, 131–142,  
632 <https://doi.org/10.1016/j.coastaleng.2014.02.009>, 2014.

633 Hu, Z., Lian, S., Wei, H., Li, Y., Stive, M., and Suzuki, T.: Laboratory data on wave propagation through  
634 vegetation with following and opposing currents, *Earth Syst. Sci. Data*, 13, 4987–4999,  
635 <https://doi.org/10.5194/essd-13-4987-2021>, 2021.

636 Huai, W., Li, S., Katul, G. G., Liu, M., and Yang, Z.: Flow dynamics and sediment transport in vegetated  
637 rivers: A review, *J Hydrodyn*, 33, 400–420, <https://doi.org/10.1007/s42241-021-0043-7>, 2021.

638 Jacobsen, N. G., Bakker, W., Uijtewaal, W. S. J., and Uittenbogaard, R.: Experimental investigation of the  
639 wave-induced motion of and force distribution along a flexible stem, *J. Fluid Mech.*, 880, 1036–1069,  
640 <https://doi.org/10.1017/jfm.2019.739>, 2019.

641 Jalonen, J. and Järvelä, J.: Impact of tree scale on drag: Experiments in a towing tank, in: *Proceedings of*  
642 *2013 IAHE world Congress*, 2013.

643 Keulegan, G. H. and Carpenter, L. H.: Forces on cylinders and plates in an oscillating fluid, *J. RES. NATL.*  
644 *BUR. STAN.*, 60, 423, <https://doi.org/10.6028/jres.060.043>, 1958.

645 Knutson, P. L., Brochu, R. A., Seeling, W. N., and Margaret, I.: Wave damping in *Spartina alterniflora*  
646 marsh, *Wetlands*, 2, 87–104, 1982.

647 Lei, J. and Nepf, H.: Blade dynamics in combined waves and current, *Journal of Fluids and Structures*, 87,  
648 137–149, <https://doi.org/doi:10.1016/j.jfluidstructs.2019.03.020>, 2019a.

649 Lei, J. and Nepf, H.: Wave damping by flexible vegetation: Connecting individual blade dynamics to the  
650 meadow scale, *Coastal Engineering*, 147, 138–148, <https://doi.org/10.1016/j.coastaleng.2019.01.008>,  
651 2019b.

652 Lei, J. and Nepf, H.: Evolution of flow velocity from the leading edge of 2-D and 3-D submerged canopies,  
653 *J. Fluid Mech.*, 916, A36, <https://doi.org/10.1017/jfm.2021.197>, 2021.

654 Li, C. W. and Yan, K.: Numerical investigation of wave–current–vegetation interaction, *Journal of*  
655 *Hydraulic Engineering*, 133, 794–803, [https://doi.org/10.1061/\(ASCE\)0733-9429\(2007\)133:7\(794\)](https://doi.org/10.1061/(ASCE)0733-9429(2007)133:7(794)),  
656 2007.

657 Losada, I. J., Maza, M., and Lara, J. L.: A new formulation for vegetation-induced damping under combined  
658 waves and currents, *Coastal Engineering*, 107, 1–13, <https://doi.org/10.1016/j.coastaleng.2015.09.011>,  
659 2016.

660 Lowe, R. J., Koseff, J. R., and Monismith, S. G.: Oscillatory flow through submerged canopies: 1. Velocity  
661 structure, *Journal of Geophysical Research: Oceans*, 110, <https://doi.org/10.1029/2004JC002788>, 2005.

662 Luhar, M. and Nepf, H. M.: Flow-induced reconfiguration of buoyant and flexible aquatic vegetation,  
663 *Limnol. Oceanogr.*, 56, 2003–2017, <https://doi.org/10.4319/lo.2011.56.6.2003>, 2011.

664 Luhar, M. and Nepf, H. M.: Wave induced dynamics of flexible blades, *Journal of Fluids and Structures*,  
665 61, 20–41, <https://doi.org/10.1016/j.jfluidstructs.2015.11.007>, 2016.

666 Mattis, S. A., Kees, C. E., Wei, M. V., Dimakopoulos, A., and Dawson, C. N.: Computational model for  
667 wave attenuation by flexible vegetation, *J. Waterway, Port, Coastal, Ocean Eng.*, 145, 04018033,  
668 [https://doi.org/10.1061/\(ASCE\)WW.1943-5460.0000487](https://doi.org/10.1061/(ASCE)WW.1943-5460.0000487), 2019.

669 Maza, M., Lara, J. L., Losada, I. J., Ondiviela, B., Trinogga, J., and Bouma, T. J.: Large-scale 3-D  
670 experiments of wave and current interaction with real vegetation. Part 2: Experimental analysis, *Coastal*  
671 *Engineering*, 106, 73–86, <https://doi.org/10.1016/j.coastaleng.2015.09.010>, 2015.

672 Monismith, S. G.: Stokes drift: theory and experiments, *J. Fluid Mech.*, 884, F1,  
673 <https://doi.org/10.1017/jfm.2019.891>, 2020.

674 Morison, J. R., Johnson, J. W., and Schaaf, S. A.: The force exerted by surface waves on piles, *Journal of*  
675 *Petroleum Technology*, 2, 149–154, <https://doi.org/10.2118/950149-G>, 1950.

676 Mullarney, J. C. and Henderson, S. M.: Wave-forced motion of submerged single-stem vegetation, *J.*  
677 *Geophys. Res.*, 115, C12061, <https://doi.org/10.1029/2010JC006448>, 2010.

678 Nepf, H. M.: Flow and transport in regions with aquatic vegetation, *Annu. Rev. Fluid Mech.*, 44, 123–142,  
679 <https://doi.org/10.1146/annurev-fluid-120710-101048>, 2012.

680 Paul, M., Bouma, T., and Amos, C.: Wave attenuation by submerged vegetation: combining the effect of  
681 organism traits and tidal current, *Mar. Ecol. Prog. Ser.*, 444, 31–41, <https://doi.org/10.3354/meps09489>,  
682 2012.

683 Pidgeon, E.: Carbon sequestration by coastal marine habitats: Important missing sinks, in: *The Management*  
684 *of Natural Coastal Carbon Sinks*, 2009.

685 Schoutens, K., Heuner, M., Minden, V., Schulte Ostermann, T., Silinski, A., Belliard, J.-P., and  
686 Temmerman, S.: How effective are tidal marshes as nature-based shoreline protection throughout  
687 seasons, *Limnol. Oceanogr.*, 64, 1750–1762, <https://doi.org/10.1002/lno.11149>, 2019.

688 Schoutens, K., Heuner, M., Fuchs, E., Minden, V., Schulte-Ostermann, T., Belliard, J.-P., Bouma, T. J.,  
689 and Temmerman, S.: Nature-based shoreline protection by tidal marsh plants depends on trade-offs  
690 between avoidance and attenuation of hydrodynamic forces, *Estuarine, Coastal and Shelf Science*, 236,  
691 106645, <https://doi.org/10.1016/j.ecss.2020.106645>, 2020.

692 Schoutens, K., Luys, P., Heuner, M., Fuchs, E., Minden, V., Schulte Ostermann, T., Bouma, T., Van Belzen,  
693 J., and Temmerman, S.: Traits of tidal marsh plants determine survival and growth response to  
694 hydrodynamic forcing: implications for nature-based shoreline protection, *Mar. Ecol. Prog. Ser.*, 693,  
695 107–124, <https://doi.org/10.3354/meps14091>, 2022.

696 Schutten, J. and Davy, A. J.: Predicting the hydraulic forces on submerged macrophytes from current  
697 velocity, biomass and morphology, *Oecologia*, 123, 445–452, <https://doi.org/10.1007/s004420000348>,  
698 2000.

699 Smith, J. M., Bryant, M. A., and Wamsley, T. V.: Wetland buffers: numerical modeling of wave dissipation  
700 by vegetation, *Earth Surf. Process. Landforms*, 41, 847–854, <https://doi.org/10.1002/esp.3904>, 2016.

701 Tang, X., Lin, P., Liu, P. L. -F., and Liu, X.: Numerical and experimental studies of turbulence in vegetated  
702 open-channel flows, *Environmental Fluid Mechanics*, 2021.

703 van Veelen, T. J., Fairchild, T. P., Reeve, D. E., and Karunarathna, H.: Experimental study on vegetation  
704 flexibility as control parameter for wave damping and velocity structure, *Coastal Engineering*, 157,  
705 103648, <https://doi.org/10.1016/j.coastaleng.2020.103648>, 2020.

706 Vuik, V., Jonkman, S. N., Borsje, B. W., and Suzuki, T.: Nature-based flood protection: The efficiency of  
707 vegetated foreshores for reducing wave loads on coastal dikes, *Coastal Engineering*, 116, 42–56,  
708 <https://doi.org/10.1016/j.coastaleng.2016.06.001>, 2016.

709 Whittaker, P., Wilson, C., Aberle, J., Rauch, H. P., and Xavier, P.: A drag force model to incorporate the  
710 reconfiguration of full-scale riparian trees under hydrodynamic loading, *Journal of Hydraulic Research*,  
711 51, 569–580, <https://doi.org/10.1080/00221686.2013.822936>, 2013.

712 Xu, Y. and Nepf, H.: Measured and predicted turbulent kinetic energy in flow through emergent vegetation  
713 with real plant morphology, *Water Resour. Res.*, 56, <https://doi.org/10.1029/2020WR027892>, 2020.

714 Yin, Z., Wang, Y., Liu, Y., and Zou, W.: Wave attenuation by rigid emergent vegetation under combined  
715 wave and current flows, *Ocean Engineering*, 213, 107632,  
716 <https://doi.org/10.1016/j.oceaneng.2020.107632>, 2020.

717 Ysebaert, T., Yang, S., Zhang, L., He, Q., Bouma, T. J., and Herman, P. M. J.: Wave attenuation by two  
718 contrasting ecosystem engineering salt marsh macrophytes in the intertidal pioneer zone, *Wetlands*, 31,  
719 1043–1054, <https://doi.org/10.1007/s13157-011-0240-1>, 2011.

720 Zeller, R. B., Zarama, F. J., Weitzman, J. S., and Koseff, J. R.: A simple and practical model for combined  
721 wave-current canopy flows, *J. Fluid Mech.*, 767, 842–880, <https://doi.org/10.1017/jfm.2015.59>, 2015.

722 Zhang, X. and Nepf, H.: Flow-induced reconfiguration of aquatic plants, including the impact of leaf  
723 sheltering, *Limnology and Oceanography*, 65, 2697–2712, <https://doi.org/org/10.1002/lno.11542>, 2020.

724 Zhang, X. and Nepf, H.: Wave damping by flexible marsh plants influenced by current, *Phys. Rev. Fluids*,  
725 6, 100502, <https://doi.org/10.1103/PhysRevFluids.6.100502>, 2021a.

726 Zhang, X. and Nepf, H.: Wave-induced reconfiguration of and drag on marsh plants, *Journal of Fluids and*  
727 *Structures*, 100, 103192, <https://doi.org/10.1016/j.jfluidstructs.2020.103192>, 2021b.

728 Zhang, X. and Nepf, H.: Reconfiguration of and drag on marsh plants in combined waves and current,  
729 *Journal of Fluids and Structures*, 110, 103539, <https://doi.org/10.1016/j.jfluidstructs.2022.103539>, 2022.

730 Zhang, X., Lin, P., Gong, Z., Li, B., and Chen, X.: Wave attenuation by *Spartina alterniflora* under macro-  
731 tidal and storm surge conditions, *Wetlands*, 40, 2151–2162, [https://doi.org/10.1007/s13157-020-01346-](https://doi.org/10.1007/s13157-020-01346-w)  
732 [w](https://doi.org/10.1007/s13157-020-01346-w), 2020.

733 Zhang, X., Lin, P., and Nepf, H.: A simple wave damping model for flexible marsh plants, *Limnology and*  
734 *Oceanography*, 66, 4182–4196, <https://doi.org/doi:10.1002/lno.11952>, 2021.

735 Zhang, X., Lin, P., and Nepf, H.: A wave damping model for flexible marsh plants with leaves considering  
736 linear to weakly nonlinear wave conditions, *Coastal Engineering*, 175, 104124,  
737 <https://doi.org/10.1016/j.coastaleng.2022.104124>, 2022.

738 Zhao, C., Tang, J., and Shen, Y.: Experimental study on solitary wave attenuation by emerged vegetation  
739 in currents, *Ocean Engineering*, 220, 108414, <https://doi.org/10.1016/j.oceaneng.2020.108414>, 2020.

740 Zhu, L., Zou, Q., Huguenard, K., and Fredriksson, D. W.: Mechanisms for the asymmetric motion of  
741 submerged aquatic vegetation in waves: A consistent-mass cable model, *J. Geophys. Res. Oceans*, 125,  
742 e2019JC015517, <https://doi.org/10.1029/2019JC015517>, 2020.

743 Zhu, L., Chen, Q., Ding, Y., Jafari, N., Wang, H., and Johnson, B. D.: Towards a unified drag coefficient  
744 formula for quantifying wave energy reduction by salt marshes, *Coastal Engineering*, 180, 104256,  
745 <https://doi.org/10.1016/j.coastaleng.2022.104256>, 2023.

746